High-resolution study of the $K\beta_2$ x-ray spectra of mid-Z atoms bombarded with 20-MeV/amu ^{12}C ions

J. Rzadkiewicz,* D. Chmielewska, and Z. Sujkowski
The Andrzej Sołtan Institute for Nuclear Studies, 05-400 Swierk, Poland

J.-Cl. Dousse, D. Castella, D. Corminboeuf, J. Hoszowska,† and P.-A. Raboud
Physics Department, University of Fribourg, CH-1700 Fribourg, Switzerland

M. Polasik and K. Słabkowska
Faculty of Chemistry, Nicholas Copernicus University, 87-100 Toruń, Poland

M. Pajek
Institute of Physics, Akademia Świetokrzyska, 25-405 Kielce, Poland
(Received 24 April 2003; published 16 September 2003)

The $K\beta_2$ x-ray spectra of zirconium, niobium, molybdenum, and palladium targets bombarded with 20.8-MeV/amu ^{12}C ions were measured with a high-resolution transmission-type bent crystal spectrometer. Well resolved M^1 and M^2 satellite lines were observed. Average M-shell and $3s,p$- and $3d$-subshell ionization probabilities for nearly central collisions were deduced. These values are compared with theoretical predictions from the semiclassical approximation using hydrogenlike and Dirac-Hartree-Fock wave functions. The experimental energy shifts of the $K\beta_2$ $M^{m=1,2}$ satellite lines are compared with values obtained from extensive multiconfiguration Dirac-Fock calculations.

DOI: 10.1103/PhysRevA.68.032713 PACS number(s): 34.50.Fa, 32.30.Rj, 32.70.Jz

I. INTRODUCTION

In the past years the phenomenon of ionization of inner and outer (sub)shells by charged particles has been a subject of intensive studies in both basic [1] and applied physics [2–4]. The study of multiple ionization provides rich and valuable information on the ionization mechanisms and electronic structures of multiple-vacancy states in atoms, as well as on the various electronic relaxation processes [5]. Results of ionization studies can also be used to probe the goodness and accuracy of theoretical models such as, the multiconfiguration Dirac-Fock (MCDF) [6], the plane-wave Born approximation [7], and the semiclassical approximation (SCA) [8]. In general, results of inner- and outer-shell ionization studies are useful in many disciplines, such as trace element analysis, ion implantation, plasma diagnostics, astrophysics, solid-state physics, atmospheric physics, x-ray lasers, and nuclear physics.

Regarding the M shell which is of interest in the present paper, it has to be mentioned that a precise knowledge of M-shell ionization probabilities is needed for a correct determination of the energies and relative intensities of K x-ray lines that are characterized by unresolved M satellite structures. From the known ionization probabilities, the yields of the unresolved M satellites can indeed be determined and used as fixed parameters in the fitting procedure from which more precise transition energies and intensities can then be obtained. For instance, the difficulty related to unresolved M satellites is encountered in measurements concerning the determination of the energy differences between hypersatellite and diagram $K\alpha_{1,2}$ lines [9]. A precise determination of these energy differences yields new information on the QED effects in electron-electron interaction. This provides an important input for the development of theoretical structure calculations.

The structure of a multiply ionized atom is much more complicated than that of a neutral or singly charged one due to many possible configurations, which depend on the number of electrons ejected from different orbitals. Multiple-vacancy configurations give rise to many initial and final electronic states, which may differ in their total angular momentum J. The number of allowed transitions between these states increases correspondingly. The deexcitation of an atom can be investigated by observing the x-ray or Auger-electron spectra. The K x-ray spectra consist of diagram lines, which originate from transitions characterized by a single K-shell hole in the initial state, and satellite structures, which are due to the presence of spectator holes in the L and M shells at the moment of the x-ray emission. As a consequence of the change in the electron screening of the nuclear charge, the satellite lines are shifted towards the high-energy sides of the diagram lines.

For the L-shell ionization data are rich and in general well reproduced by theory [10–14]. In contrast, data for the M-shell ionization cross sections [15–19] and ionization probabilities [20–22] are scarce and in many cases not consistent. In low-resolution x-ray spectroscopy experiments, the difficulties originate mainly from the poor fluorescence yields characterizing the M shell and from the contamination of the observed M x-ray spectra by K x rays of trace impurities in the targets. Moreover, in these experiments, the fluo-

*Electronic address: jacek@iriss.ipj.gov.pl
†Present address: European Synchrotron Radiation Facility, F-38043 Grenoble, France.

rescence, Auger, and Coster-Kronig yields are needed to calculate the final ionization probabilities and cross sections from the intensities of the observed x-ray transitions. The large uncertainties of these yields are then reflected in the errors of the final experimental values. In high-resolution measurements, the major difficulty arises from the small energy shifts of the *M* satellites that cannot be resolved in general from the parent *K* diagram lines and the complex line shape of the satellite structures. For these reasons, most of the available data concerning the *M*-shell ionization of mid-*Z* atoms were obtained from measurements of Auger-electron production cross sections [23] and electron-capture cross sections [24].

Because the energy shift of a satellite line increases with the principal quantum number of the transition electron, it is possible to resolve the *M* satellites from their parent diagram lines provided that the measured transitions involve electrons from outer shells and the measurements are performed with high-resolution instruments such as crystal spectrometers. For instance, as shown in Ref. [25], for mid-*Z* elements the *M* satellites of the $K\beta_2$ x-ray lines ($4p$-$1s$ transitions) can be clearly resolved. In this case, the energies of the *M*-shell satellites can be determined directly from the centroids of the well-separated satellite lines. Furthermore, from the relative intensities of the latter yield, the *M*-shell ionization probabilities for nearly-central collisions can be deduced. The relative intensities of the satellites are only weakly influenced by uncertainties in the fluorescence and Coster-Kronig yields. The so-derived ionization probabilities are therefore more precise than those obtained by means of other techniques.

Actually, similar high-resolution methods have been used earlier to determine the energies of $K\alpha$ and $K\beta$ *M*-shell x-ray satellites and the average *M*-shell ionization probabilities in nearly central collisions of mid-*Z* atoms with protons [22], ^{4}He [20,26], and ^{16}O ions [21,27]. In these works the energies of the diagram and satellite x-ray lines were found to be in good agreement with results from the MCDF theory, whereas the *M*-shell ionization probabilities were found to be much larger than the SCA predictions using hydrogenlike wave functions [28,29]. A better agreement was, however, observed by using an improved version of the SCA model in which the *M*-shell ionization probabilities were calculated with Dirac-Hartree-Fock electronic wave functions [30].

In the present paper, we report on a detailed analysis of the $K\beta_2$ spectra of $_{40}$Zr, $_{41}$Nb, $_{42}$Mo, and $_{46}$Pd targets bombarded by fast carbon ions. The main goal of this paper is to provide a deeper insight into the *M*-shell satellite structure and to determine the *M*-shell ionization probabilities due to the direct Coulomb interaction. The deduced M-shell ionization probabilities and average energies of the $K\beta_2\ M^{1,2}$ lines are compared with theoretical predictions. We also discuss the relative contributions of the *M* subshells to the total *M*-shell ionization probabilities and the influence of these subshell holes on the energies and shapes of the $K\beta_2\ M^1$ satellite lines.

II. EXPERIMENT

The experiment was performed at the variable energy cyclotron of the Paul Scherrer Institute (PSI), in Villigen, Switzerland. The $^{12}C^{5+}$ ions delivered by a 10-GHz CAPRICE ECR source were accelerated to the energy of 250 MeV. The beam intensity was about 200 nA.

The $K\beta_2$ x-ray spectra were measured by means of high-resolution x-ray spectroscopy using a DuMond-type curved-crystal spectrometer operated in the slit geometry [31]. In this geometry, the line shapes of the observed transitions are almost insensitive to the beam-induced thermal deformations of the target. The 0.15-mm-wide rectangular slit, located on the Rowland circle, 2 cm in front of the target, served thus as an effective source of radiation. The angle between the heavy-ion beam and the direction in which the target x-ray emission was measured was 55°, while the angle between the beam and target surface was 85°. The targets consisted of self-supporting metallic foils of natural Zr, Nb, Mo, and Pd with thicknesses of 12.7 mg/cm^2, 9.1 mg/cm^2, 9.3 mg/cm^2, and 8.8 mg/cm^2, respectively. They were mounted on a special aluminum holder.

A 1-mm-thick SiO_2 (110) crystal ($2d = 2.456\,671$ Å) was used for the diffraction of the x rays. The crystal plate was bent cylindrically to a radius of 313 cm and the effective reflecting area was about 5×5 cm^2. The $K\beta_2$ spectra were observed in first order of reflection. The Bragg angles were measured by means of an optical laser interferometer with a precision of about 0.01 arc sec. The diffracted x rays were detected with a 3 in. diameter and 1-mm-thick NaI scintillator surrounded by an anti-Compton ring. Good events were sorted by setting energy-windows in the analog-to-digital converter spectra. The energy windows were adjusted automatically by the acquisition program as a function of the Bragg angles. The heavy-ion beam intensity was monitored by means of a 13-mm^2 Si p-i-n photodiode, viewing the target through the same slit as the crystal of the spectrometer. The data were collected for each Bragg angle until a preset number of $K\alpha$,$K\beta$ x rays was obtained in the monitor detector so that each point of the high-resolution spectra corresponded to the same number of collisions.

The energy calibration of the spectrometer was performed by measuring for each target the photoinduced $K\beta_{1,3}$ and $K\beta_2$ lines on both sides of reflection and using the energies quoted by Bearden and Burr [32]. The photoinduced lines were also employed to determine the Gaussian instrumental response of the spectrometer. Depending on the target, a full width at half maximum (FWHM) instrumental broadening between 4 eV (Zr) and 7 eV (Pd) was found. This resolution permitted us to clearly separate the $K\beta_2M^0$, $K\beta_2M^1$, and $K\beta_2M^2$ lines, the first- and second-order *M* satellites being shifted by 25–30 eV and 50–60 eV, respectively, with respect to their parent diagram lines. In the photoionization measurements the targets were irradiated with the bremsstrahlung of a Au anode Coolidge x-ray tube equipped with a 1-mm-thick Be window and operated typically at 60 kV and 50 mA.

III. DATA ANALYSIS

A. Correction for the *K* absorption edge

For mid-*Z* atoms such as Zr, Nb, Mo, and Pd, the *K* absorption edges fall in the first *M*-satellite energy regions.

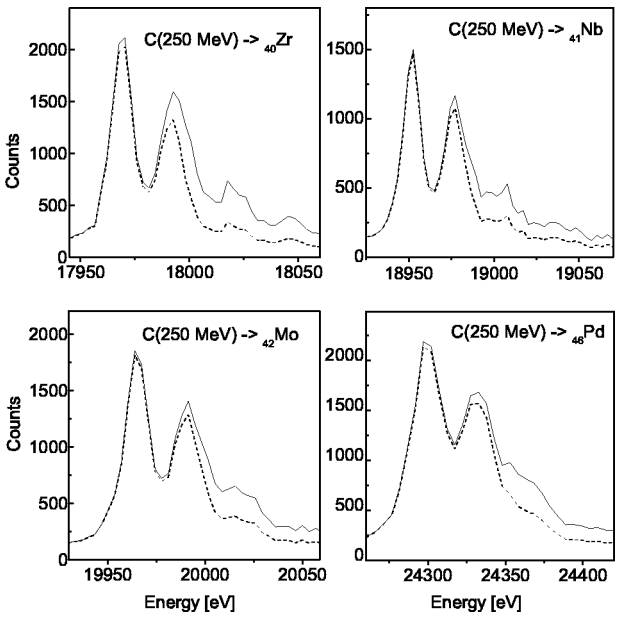

FIG. 1. High-resolution $K\beta_2$ x-ray spectra of Zr, Nb, Mo, and Pd before correction for the *K* absorption edges (dashed lines) and after (solid lines).

Therefore, the measured $K\beta_2$ spectra had to be corrected for the resulting increased self-absorption in the targets. As shown in Refs. [20,22], the corrections can be derived directly from high-resolution *K* absorption-edge measurements.

An alternative method, which was used in the present study, is to construct theoretically the shapes of the *K* absorption edges, using the known instrumental broadening of the spectrometer and the literature values [33] for the natural widths of the *K*-shell hole states. In the calculations for the *K* absorption-edge corrections, the heavy-ion-induced ionization was assumed to be constant over the entire target thickness. This assumption is reasonable since the energy losses of the heavy ions in the employed targets are small and the *K*-shell ionization cross sections can be considered as nearly constant throughout the target thickness. The effect of the calculated *K* absorption-edge corrections on the measured $K\beta_2$ x-ray spectra is depicted for the four targets in Fig. 1.

B. Fitting procedure

For singly ionized atoms the $K\beta_2$ x-ray spectrum consists of two lines, which correspond to $1s^{-1} \rightarrow 4p_{1/2}^{-1}$ and $1s^{-1} \rightarrow 4p_{3/2}^{-1}$ transitions, respectively. Since the differences in energy between these two transitions are 1.4, 1.8, 2.1, and 4.8 eV for Zr, Nb, Mo, and Pd, respectively, whereas the natural transition widths vary from about 5 eV for Zr to 12 eV for Pd, the $K\beta_2$ doublets could not be resolved in the experimental spectra.

In a doubly $K+M$ ionized atom, the additional *M*-shell vacancy reduces the nuclear charge screening. As the resulting change of the binding energy of the atomic levels decreases with the principal quantum number of the levels, the x rays emitted by such doubly ionized atoms are in general shifted towards higher energies relative to those emitted by singly ionized atoms. The shift depends on the subshell where the spectator vacancy is located. Because there are five different *M* subshells and many possibilities to couple the angular momenta of the open *M* subshell with those of the $1s$ hole in the initial state and $4p$ hole in the final state, the $K\beta_2$ M^1 satellite lines consist of numerous components which differ in energy and transition probability. As a consequence, *M*-shell satellite structures are usually very complex. For the $K\alpha_{1,2}$ $(2p\text{-}1s)$ and $K\beta_{1,3}$ $(3p\text{-}1s)$ transitions, the energy shifts of the *M* satellites are smaller than the natural widths of the transitions so that the complex *M*-satellite structures cannot be separated from the main lines. Only broadenings of the latter can be observed and shifts of their centroid energies. In this case it is thus very difficult to obtain reliable quantitative information about the energy, intensity, and line shape of the *M* satellites. More precise results can, however, be derived from the $K\beta_2$ $(4p\text{-}1s)$ transitions for which the *M* satellites can be resolved.

The measured $K\beta_2$ x-ray spectra were analyzed by means of a least-squares-fit program, using three different methods to reproduce the shapes of the complex satellite structures. In the first method, single Voigt profiles were employed to fit the diagram and satellite lines. The energy, intensity, and Lorentzian width of each Voigtian as well as a linear background were used as free fitting parameters, whereas the Gaussian width corresponding to the instrumental broadening was kept fixed at its known value. From this first step of the analysis, we obtained the experimental energy shifts of the *M*-shell satellites that are reported in Sec. IV E. They were determined from the energy differences between the centroids of the fitted Voigtians corresponding to the $K\beta_2$ $M^{1,2}$ satellites and $K\beta_2$ M^0 diagram lines. Although the complex and asymmetric shapes of the satellites could not be accurately reproduced by single Voigtian profiles, the satellite centroids were found to be well approximated by the central energies of the fitted Voigtians. In addition, this simple method presented the advantage to provide pure experimental energies, i.e., values that do not depend on any theoretical parameter.

In order to better reproduce the shapes of the experimental spectra, an improved analysis of the data was then performed, in which theoretical profiles were employed to fit the $K\beta_2$ diagram and satellite lines. The theoretical profiles were determined by means of extensive MCDF calculations (see Sec. III F). Results of MCDF calculations are stick spectra which represent the energies and relative intensities of the components pertaining to the diagram and satellite transitions. To be compared with the experimental spectra, Voigtian profiles were attached to the MCDF components and then all Voigtians corresponding to the same spectra were added together. The same Lorentzian widths were employed for all MCDF components. They were derived from the level widths reported in Ref. [33]. The Gaussian widths were let free in the fitting procedure in order to account for the unresolved *N* satellites. A further free fitting parameter was employed to anchor the MCDF energy scale to the experimental energies. An intensity scaling factor and a constant background were also used as free fitting parameters. More details about this MCDF-based data analysis can be found in

Refs. [20,22,27,34]. Assuming a binomial distribution for the number of *M*-shell holes, the average *M*-shell ionization probabilities could then be derived from the values provided by the fits for the above-mentioned intensity scaling factors. As already mentioned, the number of spectator holes and the numerous possibilities to couple them increase the number of initial and final atomic states and consequently the number of x-ray transitions. For instance, for Pd which has in its ground-state electronic configuration only complete subshells, the $K\beta_2\ M^1$ and $K\beta_2\ M^2$ satellite lines consist of 72 and 1704 components, respectively. For the remaining measured elements which have open subshells in their ground state, the number of components is significantly larger. This made the MCDF-based analysis more complicated and time consuming. On the other hand, the satellite line shapes could be reproduced more precisely than in the first analysis. The average *M*-shell ionization probabilities p_M quoted in Sec. IV C were obtained from this second stage of the data analysis.

Finally, as the energy shifts and relative intensities of the satellites depend on the *M* subshells in which the spectator holes are located, we tried in a further step to reanalyze the spectra with the MCDF method, using distinct intensity scaling factors for the different *M* subshells. The objective of this third step was thus to determine separate *M*-subshell ionization probabilities. Actually, due to the weak intensity of the satellite components associated to the $3s$ spectator holes, only two intensity scaling factors corresponding to the $3s,p$ and $3d$ subshell ionization probabilities were used as free fitting parameters. In addition, in order to keep the data analysis at a tractable level, only the $K\beta_2\ M^1$ satellite lines were analyzed with this method, the second-order $K\beta_2\ M^2$ satellites being fitted with the one-intensity parameter MCDF method described in the preceding paragraph. The $M_{\mathrm{I,II,III}}$- and $M_{\mathrm{IV,V}}$-subshell ionization probabilities discussed in Sec. IV D were obtained from this third stage of the data analysis.

C. Correction for the *M*-shell electron rearrangement

The electron rearrangement processes occurring in the ion during the time between the collision-induced *K*-shell ionization and the emission of the $K\beta_2$ x-ray transition may change the total number of *M*-shell vacancies. The $K\beta_2\ M^m$ satellite yields extracted from the fitting procedure reflect thus the *M*-hole distribution in the target atoms at the moment of the *K* x-ray emission and not the initial hole configuration induced by the interaction with the projectile. The initial number of *M*-shell holes can, however, be estimated by taking into account all those processes that modify the number of *M*-shell vacancies prior to the x-ray emission. These processes were accounted for using simple statistical scaling procedures as discussed in Refs. [22,35].

For the *M*-shell, the main rearrangement processes are the *MXY* Auger transitions which diminish the initial number of *M*-shell holes by one unit. The radiative *M* transitions which also reduce the number of M holes by one unit can be neglected because the *M*-shell fluorescence yields are small. The MMM super-Coster-Kronig transitions which increase the number of *M* holes by one unit are very weak or forbidden for mid-*Z* atoms and were therefore not considered.

The $K^{-1}\ M^{-1}$ double-vacancy states may also be produced by the decay of $K^{-1}L^{-1}$ states via radiative L^{-1}-M^{-1} transitions. However, the contribution of these second-order processes to the *M*-shell ionization being small for the investigated collisions (about 1%), they were also neglected.

The observed x-ray yields X^0 and X^1 of the $K\beta_2\ M^{1,2}$ transitions are related to the initial vacancy yields I^0 and I^1 by the following equations:

$$X^0=(I^0+RI^1)\,\omega^0_{\beta_2}, \tag{1}$$

$$X^1=(I^1-RI^1)\,\omega^1_{\beta_2}, \tag{2}$$

where R is the scaling factor describing the electron rearrangement and $\omega^0_{\beta_2}$, $\omega^1_{\beta_2}$ represent the partial fluorescence yields of the $K\beta_2$ transitions with zero, respectively, one *M*-shell spectator vacancy. The total rearrangement factor R is given by the weighted sum of the partial coefficients R_i of the different *M* subshells:

$$R=\sum_{i=1}^{5} w_i R_i\,. \tag{3}$$

Assuming equal ionization probabilities (per electron) for the *M* subshells, the weighting factors w_i can be estimated to be proportional to the numbers of electrons in the *M* subshells of the neutral atom, i.e., $w_1:w_2:w_3:w_4:w_5=2:2:4:4:6$.

The partial factors R_i, which give the probability that the *M*-subshell vacancy has been promoted to an outer (sub)shell within the lifetime of the *K*-shell hole, can be written as:

$$R_i=\frac{\Gamma_{M_i}-\sum_{i<j} f_{i,j}\Gamma_{M_iM_jX}}{\Gamma_K+\Gamma_{M_i}}, \tag{4}$$

where Γ_K and Γ_{M_i} are the total widths of the *K* and M_i atomic levels and $f_{i,j}$ relative Coster-Kronig yields. The latter were taken from Refs. [36–38] and the *K* and M_i level widths from [33]. Using this procedure the following values were obtained for the total rearrangements factors R:0.020,0.022,0.031 and 0.031 for $_{40}$Zr, $_{41}$Nb, $_{42}$Mo, and $_{46}$Pd, respectively.

Finally, if we assume the fluorescence yields of the $K\beta_2\ M^0$ and $K\beta_2\ M^1$ transitions to be the same, the initial satellite-to-diagram line yield ratios can be written as

$$i_M=\frac{I^1}{I^0}=\frac{X^1/X^0}{1-R(1+X^1/X^0)}. \tag{5}$$

D. Correction for the *M*-subshell electron rearrangement

Only those processes which modify the distribution of the *M* holes among the $M_{\mathrm{I,II,III}}$ and $M_{\mathrm{IV,V}}$ subshells and consequently affect the $3s,p$- and $3d$-subshell ionization probabilities were considered. The $M_{sp}M_dX$ Coster-Kronig tran-

sitions which transfer the $3s$ or $3p$ holes into the $3d$ subshell and produce extra holes in the N shell represent the main process for this intrashell electron rearrangement. As a consequence of the Coster-Kronig transitions, the degree of the $3s$ or $3p$ ionization at the moment of the x-ray emission is smaller than that at the moment of the ion-atom collision. The contrary is true for the $3d$ ionization. For $M_{sp}M_dX$ Coster-Kronig transitions, one hole in the $3s$ or $3p$ subshell and one electron in the $3d$ subshell must exist in the initial state. Thus, in the rearrangement calculations, the $M_{sp}M_dX$ Coster-Kronig transition probabilities have to be multiplied by the average number of $3s$ and $3p$ holes (m_{3sp}) and by the factor $(1-p_{3d})$ which is proportional to the number of $3d$ electrons. Since m_{3sp} and $(1-p_{3d})$ factors were still unknown when performing the rearrangement calculations, they were determined by an iterative procedure, using the x-ray yield ratios quoted in Table III as initial values. Finally, the probability that a $M_{sp}M_dX$ Coster-Kronig transition occurs after a $3s$ or $3p$ ionization and prior to the $K\beta_2$ x-ray emission can be written as

$$R_{3sp\rightarrow 3d}=\frac{(1-p_{3d})m_{3sp}\Gamma_{M_{sp}M_dX}}{(1-p_{3d})m_{3sp}\Gamma_{M_{sp}M_dX}+\Gamma_K}, \tag{6}$$

where $\Gamma_{M_{sp}M_dX}$ is the total width of the $M_{sp}M_dX$ Coster-Kronig transitions for singly ionized atoms and Γ_K is the K-shell width. The Coster-Kronig widths were derived from the values reported in Refs. [36–43], leading to the following subshell rearrangement factors $R_{3sp\rightarrow 3d}$: 0.15, 0.14, 0.14, and 0.13 for $_{40}$Zr, $_{41}$Nb, $_{42}$Mo, and $_{46}$Pd, respectively.

Finally, the initial vacancy yield ratios i_{3sp} and i_{3d} used for the determination of the M-subshell ionization probabilities can be expressed as

$$i_{3sp}=\frac{X^1_{3sp}(1+R_{3sp\rightarrow 3d})/X^0}{1-\sum_{i=1}^{3}\omega_i R_i[1+X^1_{3sp}(1+R_{3sp\rightarrow 3d})/X^0]}, \tag{7}$$

$$i_{3d}=\frac{X^1_{3d}(1-R_{3sp\rightarrow 3d})/X^0}{1-\sum_{i=4}^{5}\omega_i R_i[1+X^1_{3d}(1-R_{3sp\rightarrow 3d})/X^0]}. \tag{8}$$

E. Ionization probabilities

If direct uncorrelated Coulomb ionization is the main process governing the M-shell ionization, then the M-shell vacancy distribution can be described in the independent-particle approximation by the binomial distribution with the ionization probability per electron as free parameter. The probability that a collision with an impact parameter b produces exactly m vacancies in the K shell and n vacancies in the M shell can be written as

$$P_{mK,nM}(b)=\binom{2}{m}\binom{18}{n}[p_K(b)]^m[1-p_K(b)]^{2-m}\times[p_M(b)]^n[1-p_M(b)]^{18-n}, \tag{9}$$

where p_K and p_M represent the average K- and M-shell ionization probabilities per electron, respectively. The corresponding cross sections are obtained from the integration of the ionization probabilities over the impact parameter b:

$$\sigma_{mK,nM}=2\pi\int_0^\infty bP_{mK,nM}(b)db. \tag{10}$$

Since the mean M-shell ionization probability p_M is almost constant over the impact parameter range $(0,b_{\max})$, where the K-shell ionization probability is significant, one finds that

$$\frac{\sigma_{1K,1M}}{\sigma_{1K,0M}}=i_M=\frac{18p_M(0)}{1-p_M(0)}, \tag{11}$$

where $\sigma_{1K,0M}$ and $\sigma_{1K,1M}$ are the cross sections for the production of the $K^{-1}M^0$ single- and $K^{-1}M^{-1}$ double-vacancy states and I_M is the initial vacancy yield ratio. Using the relations (5) and (11), the probability for the average M-shell ionization per electron can finally be expressed as

$$p_M=\frac{i_M}{18+i_M}. \tag{12}$$

Corresponding relations for the M-subshell ionization probabilities are

$$p_{3sp}=\frac{i_{3sp}}{8+i_{3sp}}, \tag{13}$$

$$p_{3d}=\frac{i_{3d}}{10+i_{3d}}. \tag{14}$$

Relations (12), (13), and (14) do not depend on the vacancy production processes.

F. MCDF calculations

The experimental $K\beta_2$ spectra were decomposed into three groups: $K\beta_2$ M^0, $K\beta_2$ M^1, and $K\beta_2$ M^2. For each group the spectrum was constructed theoretically using the transition energies and transition probabilities determined from extensive MCDF calculations. The MCDF method which was used in the present study was already described in detail in many papers [6,44–48], so only some essential ideas are given below.

Within the MCDF scheme the effective Hamiltonian for an N-electron atom is given by the sum of the Dirac operators $h_D(i)$ and the terms C_{ij} which account for the electron-electron interactions arising from one-photon exchange processes:

$$H=\sum_{i=1}^{N}h_D(i)+\sum_{j>i=1}^{N}C_{ij}. \tag{15}$$

The C_{ij} terms are given by

$$C_{ij}=1/r_{ij}+T(r_{ij}), \tag{16}$$

where $1/r_{ij}$ is the Coulomb interaction operator (due to longitudinally polarized photons) and $T(r_{ij})$ is the transverse Breit operator (due to transversely polarized photons).

In the MCDF method an atomic state function with the total angular momentum J and parity p is assumed to have the following multiconfigurational form:

$$\Psi_s(J^p)=\sum_m^{N_c} c_m(s)\Phi(\gamma_m J^p), \tag{17}$$

where $\Phi(\gamma_m J^p)$ are configuration state functions (CSF's), i.e., the antisymmetrized products of one-electron spinors of specified angular symmetry labeled by J and parity p; N_c is the number of CSF's included in the expansion; $c_m(s)$ are configuration mixing coefficients for state s; and γ_m represents the information required to uniquely define a certain CSF.

Various versions of MCDF calculations were developed, depending on the choice of the form of the energy functional [45,47–51]. In order to make the MCDF calculations for the $K\beta_2$ transitions of mid-Z atoms as reliable as possible, in the present study we use the modified special average-level version of MCDF calculations (MCDF-MSAL), proposed in Ref. [48]. In this version the energy functional is expressed by

$$E=E_{opt}+\sum_a \overline{q_a}\epsilon_a S(a,a)+\sum_{\substack{a,b\\ a\neq b}} \epsilon_{a,b}S(a,b), \tag{18}$$

where $\overline{q_a}$ is the generalized occupation number for the orbital a, ϵ_a and ϵ_{ab} are the Lagrange multipliers, $S(a,b)$ is the overlap integral, and E_{opt} is taken in the form

$$E_{opt}=\frac{1}{\lambda+1}\left[\frac{\lambda}{n_i}\sum_{i=1}^{n_i} H_{ii}+\frac{1}{n_f}\sum_{f=1}^{n_f} H_{ff}\right], \tag{19}$$

where H_{ii} and H_{ff} are the diagonal contributions to the Hamiltonian matrix, the first sum runs over all initial CSF's (n_i), the second one over all final CSFs (n_f), and λ is a factor which accounts in a simple way for the difference in quality of the description of the initial and final states.

One can see that if $\lambda=1$ one obtains a formula in which the compensation for the exaggerated contribution of the more numerous states (initial or final) to the energy functional is complete [48]. This result is a good reproduction of the relative positions of the spectral lines. However, for $\lambda=1$ the calculated diagram and satellite line energies for the transitions $K\alpha_{1,2}\,L^lM^m$, $K\beta_{1,3}\,L^lM^m$, and $K\beta_2\,L^lM^m$ are shifted with respect to the experimental ones by similar amounts [48]. The optimum values of λ depend strongly on the spectral line type, but they are almost independent of the type of atoms. It was found [48] that the experimental energies of the diagram and satellite lines of mid-Z atoms are well reproduced by the formula (19) if values of 0.5, 0.65, and 0.8 are chosen for λ for the $K\alpha_{1,2}\,L^lM^m$, $K\beta_{1,3}\,L^lM^m$, and $K\beta_2\,L^lM^m$ transitions, respectively. The above functional has already been applied with success in the extensive MCDF study on the structure of $K\alpha_{1,2}\,L^lM^m$, $K\beta_{1,3}\,L^lM^m$, and $K\beta_2\,L^lM^m$ satellite lines in the x-ray spectra of mid-Z atoms induced in near-central collisions with various light and heavy projectiles [20–22,26,27,34].

In the present study, we have used the computer program package GRASP [46] which allows to include the Breit interaction and QED (self-energy and vacuum polarization) corrections in the MCDF calculations. The following outer-shell electronic configurations were employed: $4d^25s^2$ for Zr, $4d^45s^1$ for Nb, $4d^45s^2$ for Mo, and $4d^{10}$ for Pd.

IV. RESULTS AND DISCUSSION

A. Theoretical shapes of the $K\beta_2$ spectra

A proper interpretation of the experimental $K\beta_2$ x-ray spectra corresponding to the multiple ionization of mid-Z atoms by fast heavy ions requires a good theoretical knowledge of the structure of the diagram and satellite x-ray lines occurring in the spectra. Therefore, the extensive MCDF calculations (see Sec. III F) were carried out for each target element. Depending on the number and location of the spectator vacancies, the $K\beta_2$ transitions can be divided into various groups of lines such as the $K\beta_2L^0M^0$ diagram, $K\beta_2\,L^0M^1$, $K\beta_2\,L^0M^2$, $K\beta_2\,L^1M^0$, and $K\beta_2\,L^1M^1$ satellite lines, etc.

The $K\beta_2\,L^0M^{0,1}$ theoretical spectra corresponding to the four measured elements are presented in Figs. 2–5. They

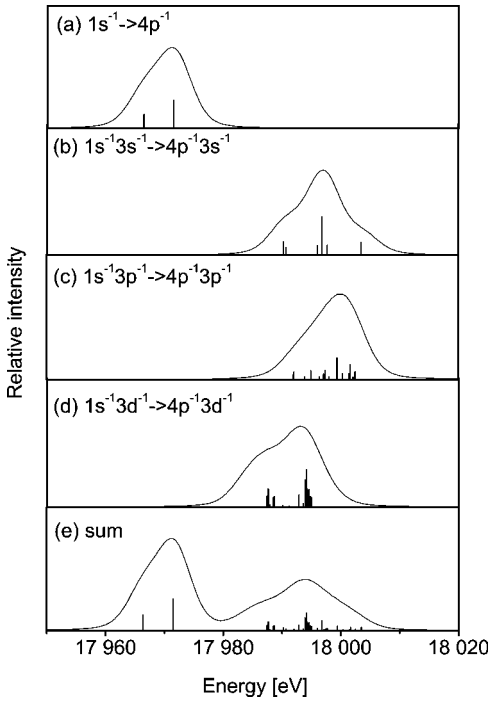

FIG. 2. MCDF theoretical profiles of the $1s$-$4p$ transition of Zr with (a) no spectator vacancy, respectively, one spectator vacancy in the (b) $3s$ level, (c) $3p$ level, and (d) $3d$ level. The profile depicted in (e) is the sum of the components (a)–(d). Each stick spectrum was normalized so that the sum of the transition probabilities is equal to 1. To be compared with the experiment, the satellite part of the profile (e) must be multiplied by the total M-shell ionization probability.

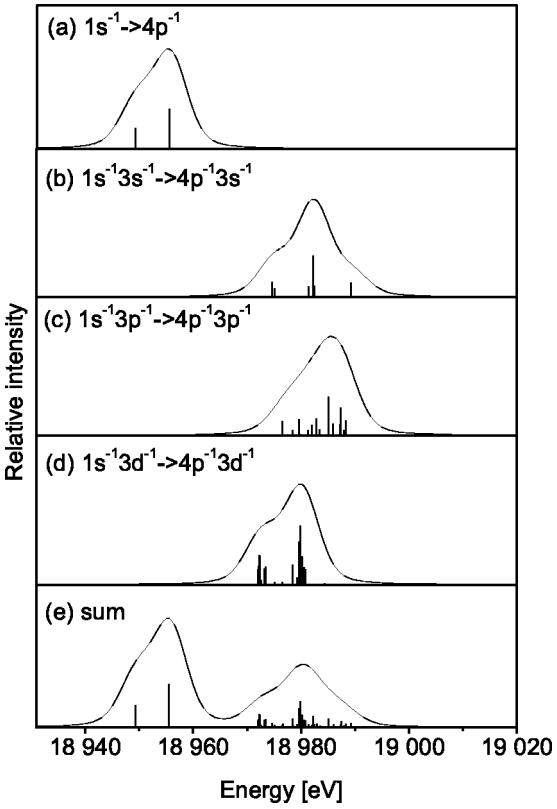

FIG. 3. Same as Fig. 2 but for Nb.

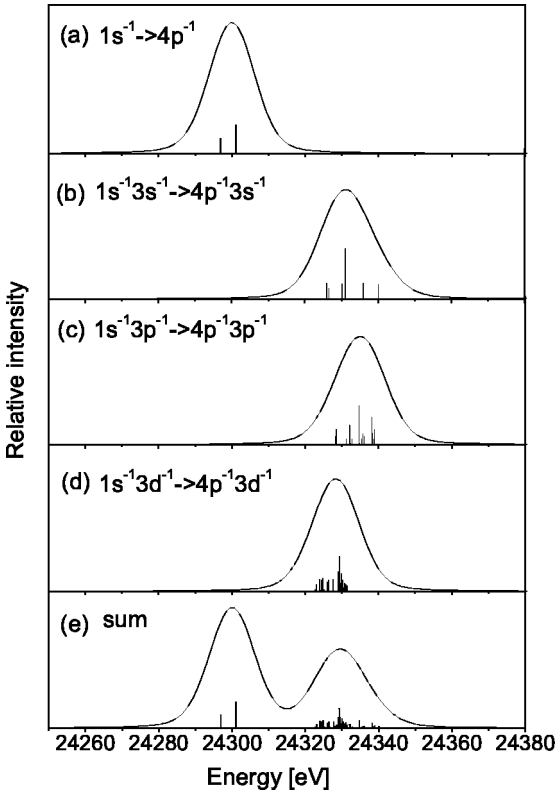

FIG. 5. Same as Fig. 2 but for Pd.

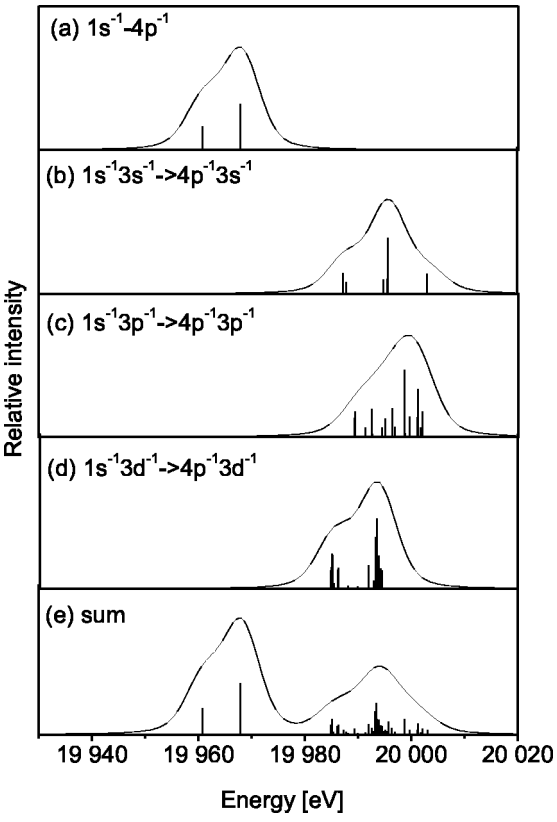

FIG. 4. Same as Fig. 2 but for Mo.

were constructed as described before, using Lorentzian widths of 4.6, 5.3, 6.3, and 12.1 eV and Gaussian widths of 5.5, 6.0, 6.5, and 8.6 eV, respectively, for Zr, Nb, Mo, and Pd.

The $K\beta_2$ L^0M^0 diagram lines, which correspond to the transitions ($1s^{-1} \rightarrow 4p^{-1}_{1/2,3/2}$) with all other electronic states occupied, were constructed first. Results are shown in Figs. 2(a)–5(a). The energy difference between the two diagram line components ranges from 5.1 eV for $_{40}$Zr to 7.1 eV for $_{42}$Mo, but falls down to 4.1 eV for $_{46}$Pd. This smaller energy difference combined with the longer Lorentzian and Gaussian widths associated to the Pd lines explains why the $K\beta_2$ spectrum of this element [see Fig. 5(a)] looks more symmetric than that of the three other targets.

In the case of the $K\beta_2$ L^0M^1 satellite lines, three groups of transitions were considered: $1s^{-1}3s^{-1} \rightarrow 4p^{-1}3s^{-1}$, $1s^{-1}3p^{-1} \rightarrow 4p^{-1}3p^{-1}$, and $1s^{-1}3d^{-1} \rightarrow 4p^{-1}3d^{-1}$. The energy differences between neighboring lines in the $3p$ and $3d$ groups are smaller than in the $3s$ group.

As a consequence, the $3s$ ($1s^{-1}3s^{-1} \rightarrow 4p^{-1}3s^{-1}$) line shapes [see Figs. 2(b)–5(b)] look somewhat less smooth than those corresponding to the $3p$ and $3d$ satellite lines. For Zr, Nb, and Mo asymmetries are observed in the profiles corresponding to the transitions with additional $3p$ [see Figs. 2(c)–4(c)] and $3d$ holes [see Figs. 2(d)–4(d)]. For the same reasons as those discussed for the diagram line, these asymmetries are not visible for Pd [see Figs. 5(c) and 5(d)]. Finally, for all targets, it can be noted that the $3s$ and $3p$ satellites are more shifted towards higher energies than the $3d$ ones.

B. Relevant *M*-shell ionization processes for collisions with fast ^{12}C ions

With the satellite technique employed in the present study, only those excitation processes that produce $K^{-1}M^{-m}$ multivacancy states have to be considered. The most important one is certainly the direct Coulomb ionization. In this process, due to the Coulomb interaction between the charged projectiles and the *K*- and *M*-shell target atom electrons, the latter are excited from their bound states into the continuum. Several other processes may also contribute, to a smaller extent, to the production of $K^{-1}M^{-m}$ multivacancy states. Such competitive processes are shake-up and shake-off, radiative and nonradiative electron capture and internal conversion of γ rays following Coulomb nuclear excitation. However, except shake-up and shake-off which are discussed below, other processes can be neglected because their cross sections are several orders of magnitude smaller than the direct Coulomb ionization cross section [52–55].

In a shake process, as a result of the sudden change of the atomic potential caused by the removal of a *K*-shell electron, one or even several *M*-shell electrons can be promoted to higher unfilled orbitals (shake-up) or excited into the continuum (shake-off) [56–58]. Actually, the *M*-shell shake probabilities for mid-*Z* atoms are rather small and only the yields of the first-order *M* satellites may contain nonnegligible contributions from shake processes. Furthermore, the shake probabilities do not depend on the mechanism leading to the creation of the 1*s* vacancies. As a consequence, *M* satellites originating from shake processes are also present in the photoinduced *K* x-ray spectra and their intensities are the same as those one would observe in the heavy-ion-induced spectra in the absence of the direct Coulomb ionization process. In addition, since in photoinduced *K* x-ray spectra the *M*-shell spectator vacancies result exclusively from shake-off and shake-up processes, the contributions of the latter to the *M*-satellite yields observed in the heavy-ion-induced spectra can be deduced straightforwardly from the measured intensities of the photoinduced $K\beta_2\ M^1$ satellites.

Shake probabilities can also be calculated using the so-called sudden-approximation model (SA) [57,59,60]. In general, however, results of such calculations underestimate the experimental probabilities. For instance, for Ar experimental *M*-shell shake probabilities following 1*s* photoionization are larger by about 10% than the SA predictions, whereas for Kr the deviation is still more [about (50%)] [61]. For Zr, Mo, and Pd, the experimental shake probabilities derived from the relative yields of photoinduced $K\beta_2\ M^1$ satellites were found to be up to three times larger than the values predicted by the SA model [22]. A similar big discrepancy was observed for pure metallic Mo and Mo compounds [62]. In these former studies, the discrepancies were attributed to the quadrupole-allowed $K\beta_4$ $(4d\text{-}1s)$ transitions which are overlapping with the $K\beta_2\ M^1$ satellite lines and have strongly enhanced intensities as a result of solid-state effects.

C. Average *M*-shell ionization probability

The X^1 $(K\beta_2\ M^1)$ to $X^0(K\beta_2\ M^0)$ x-ray yield ratios obtained from the second step of the fitting procedure (see Sec. III B) are given in Table I. For comparison, similar x-ray yield ratios obtained in former experiments with photons, protons, and α particles are also presented. The data were not corrected for the intensity of the overlapping $K\beta_4$ transitions. It can be noted that the ratios obtained after subtraction of the values labeled *photo*, which correspond to the shake plus $K\beta_4$ contributions, vary almost linearly with the squared charge of the projectiles, as predicted by theory. Furthermore, for collisions with ^{12}C ions, ratios close to 1 are observed. Assuming a binomial distribution for the *M*-shell holes, this ratio of about 1 indicates that there is an average of approximately one *M*-shell hole per collided target atom at the moment of the *K* x-ray emission.

TABLE I. $K\beta_2\ M^1$ satellite to $K\beta_2\ M^0$ diagram line yield ratios (in %) observed as a result of photon, 25-MeV proton, 25-MeV/amu α particle, and 20-MeV/amu ^{12}C ion bombardment. Rearrangement processes were not accounted for in the quoted values, which reflect thus the relative number of doubly ionized atoms at the moment of the *K* x-ray emission.

Element	Photo[a]	25-MeV p[a]	100-MeV α[b]	250-MeV C
$_{40}$Zr	8.39(35)	7.03(67)	16.9(1.6)[b]	108(20)
$_{41}$Nb				104(26)
$_{42}$Mo	8.60(36)	6.27(46)	13.6(0.7)[b]	98(17)[c]
$_{46}$Pd	2.46(24)	2.73(33)	6.1(0.4)[b]	86(11)

[a]Taken from Ref. [22].
[b]Taken from Ref. [20].
[c]Taken from Ref. [63].

The x-ray yield ratios (X^1/X^0) resulting from the direct Coulomb ionization process alone can be obtained as follows:

$$\frac{X^1}{X^0}=\left[\frac{I(K\beta_2\ M^1)}{I(K\beta_2\ M^0)}\right]_{^{12}\mathrm{C}}-\left[\frac{I(K\beta_2\ M^1}{I(K\beta_2\ M^0)}\right]_X, \qquad (20)$$

where $[I(K\beta_2\ M^1)/I(K\beta_2 M^0)]_{^{12}\mathrm{C}}$ and $[I(K\beta_2\ M^1/I(K\beta_2\ M^0)]_X$ are the ratios derived from the ^{12}C-induced and photoinduced $K\beta_2$ spectra. For Nb, the ratio $[I(K\beta_2\ M^1/I(K\beta_2\ M^0)]_X$ was determined from a linear interpolation of the values quoted for Zr and Mo (see Table I).

Introducing these new ratios in Eq. (5) and using then Eq. (12), one obtains the experimental average *M*-shell ionization probabilities per electron listed in Table II. As the latter

TABLE II. Experimental and theoretical (SCA model) average *M*-shell ionization probabilities per electron for mid-*Z* targets bombarded by 20.8-MeV/amu C ions.

Element	Expt.	SCA-HYD	SCA-DHF
$_{40}$Zr	0.054(11)	0.010	0.041
$_{41}$Nb	0.052(14)	0.010	0.039
$_{42}$Mo	0.050(9)	0.011	0.039
$_{46}$Pd	0.047(7)	0.010	0.040

were determined with the satellite technique, the observed *M*-shell ionization is obligatorily accompanied by a simultaneous *K*-shell ionization. In other words, the results quoted in Table II are only valid for collisions that are nearly central in the *M*-shell scale. In addition, as discussed above, they only reflect the *M*-shell vacancies produced by the direct Coulomb ionization process.

For comparison, theoretical *M*-shell ionization probabilities are also presented in Table II. They were computed using the SCA. The SCA model is based on the first-order perturbation theory. This theory is especially useful for the description of the impact-parameter-dependent single-electron ionization probabilities for fast asymmetric ion-atom collisions ($Z_P < Z_T$). The SCA theory was introduced and developed by Bang, Hansteen, and co-workers [8] and successfully used in the description of the *K*- and *L*-shell ionization [64–66].

The present calculations for the *M* shell were performed by means of the SCA version of Trautmann and Rösel [28,29]. The *M*-shell ionization probabilities were calculated with the use of both relativistic hydrogenlike wave functions (SCA-HYD) and Dirac-Hartree-Fock (SCA-DHF) wave functions. The wave functions for the bound *M*-shell electrons were computed using the GRASP program, whereas the wave functions for the electrons in the continuum were computed using the code CONTWVG developed by Halabuka *et al.* [30]. For each target, the calculations were performed for an impact parameter of $b_K^{eff} = 500$ fm. Hyperbolic projectile paths were used and the recoil effect of the nucleus was included in the calculations. The united atom picture was employed and multipole terms up to $L = 6$ were considered.

The theoretical *M*-shell ionization probabilities quoted in Table II correspond to weighted average values of the *M*-subshell ionization probabilities, the statistical weights being proportional to the number of electrons in the subshells. The experimental errors are due to the uncertainties on the fitted *M*-satellite yields and rearrangement processes.

Comparing the experimental probabilities with the theoretical ones, one sees first that the SCA-HYD values strongly underestimate the experimental results (up to a factor of 5). In contrast to that, a better agreement is observed with the SCA-DHF predictions, although there is a systematic trend of the experimental data to be slightly larger than the calculated values. Similar differences between theory and experiment were observed in earlier experiments using 24.8-MeV/amu He projectiles [20]. The variation of the experimental to theoretical *M*-shell ionization probability ratio as a function of the target atomic number is presented in Fig. 6. One can see that for both the present experiment and the He one, a drastic improvement of the theoretical predictions is observed when Dirac-Hartree-Fock wave functions are used instead of relativistic hydrogenlike ones, and that the *Z*-dependent deviation between experiment and theory observed with the SCA-HYD model seems to vanish in the SCA-DHF one.

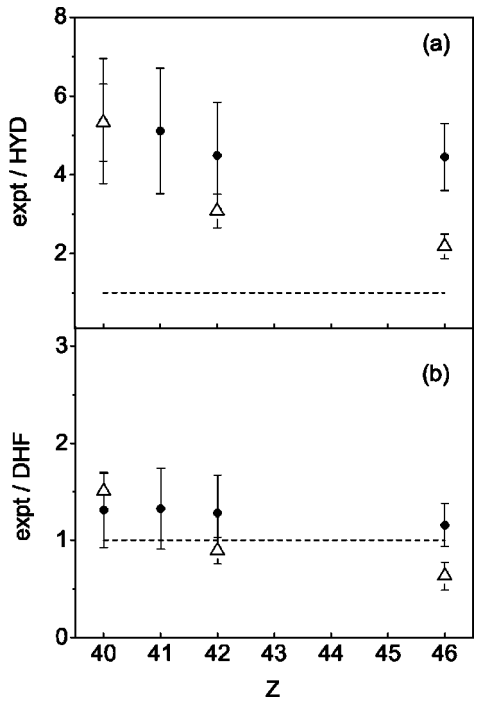

FIG. 6. Ratio of experimental to (a) SCA-HYD and (b) SCA-DHF theoretical *M*-shell ionization probabilities per electron as a function of the target atomic number for (●) collisions with 20.8-MeV/amu C (present work) and (△) 25-MeV/amu He [20] ions. The dashed lines correspond to ratios of 1.

D. *M*-subshell ionization probabilities

The ionization probabilities and rearrangement processes corresponding to different *M* subshells may differ largely, because of the differences in the binding energies of the $3s$, $3p$, and $3d$ electrons and shapes of their wave functions. Therefore the fitting procedure using a single parameter for the *M*-shell ionization probability can be improved by the introduction of two independent parameters p_{3sp} and p_{3d}, which represent the ionization probabilities per electron for the $3s,p$ and $3d$ subshells, respectively (see Sec. III B). Using this improved fitting procedure, it was possible to better reproduce the shapes of the $K\beta_2$ M^1 satellites (see Figs. 7–10).

The *M*-subshell satellite-to-diagram line yield ratios were determined from the fitted relative intensities of the X^1_{3sp}, X^1_d, and X^0 components. As the shake and $K\beta_4$ transition contributions are still included in these ratios, the latter were corrected to correspond to the sole direct Coulomb ionization process, using the following equations:

$$\frac{X^1_{3sp}}{X^0} = \left[\frac{I(K\beta_2\ M^1_{3sp})}{I(K\beta_2\ M^0)}\right]_{^{12}\mathrm{C}} - \left[\frac{I(K\beta_2\ M^1_{3sp})}{I(K\beta_2\ M^0)}\right]_X, \quad (21)$$

$$\frac{X^1_{3d}}{X^0} = \left[\frac{I(K\beta_2\ M^1_{3d})}{I(K\beta_2\ M^0)}\right]_{^{12}\mathrm{C}} - \left[\frac{I(K\beta_2\ M^1_{3d})}{I(K\beta_2\ M^0)}\right]_X, \quad (22)$$

where

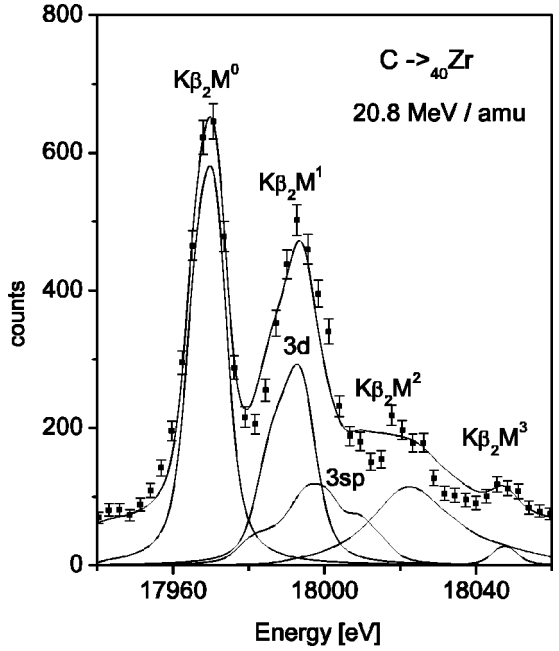

FIG. 7. Comparison between the measured and fitted $K\beta_2$ spectra for 250-MeV C impact on Zr. The solid line represents the total fit, while the lines labeled $3sp$ and $3d$ stand for the fitted satellite components corresponding to one spectator vacancy in the $3s$ or $3p$ and $3d$ levels, respectively.

$$[I(K\beta_2\ M^1_{3sp})/I(K\beta_2\ M^0)]_{^{12}\mathrm{C}},$$

$$[I(K\beta_2\ M^1_{3d})/I(K\beta_2\ M^0)]_{^{12}\mathrm{C}},$$

$$[I(K\beta_2\ M^1_{3sp})/I(K\beta_2\ M^0)]_X,$$

and

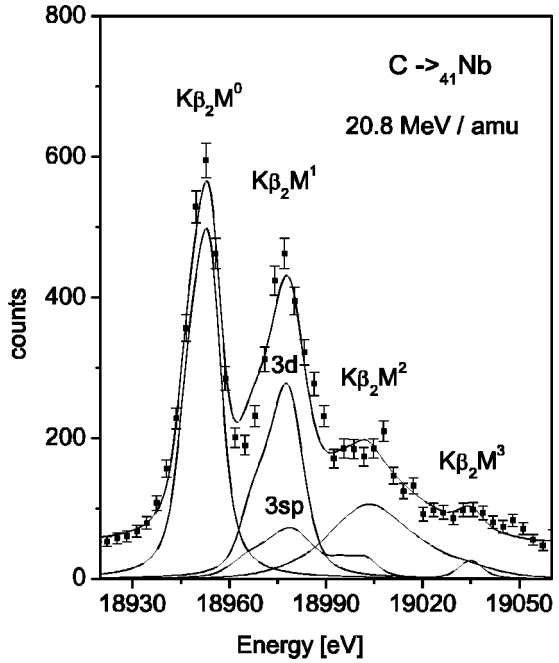

FIG. 8. Same as Fig. 7 but for Nb.

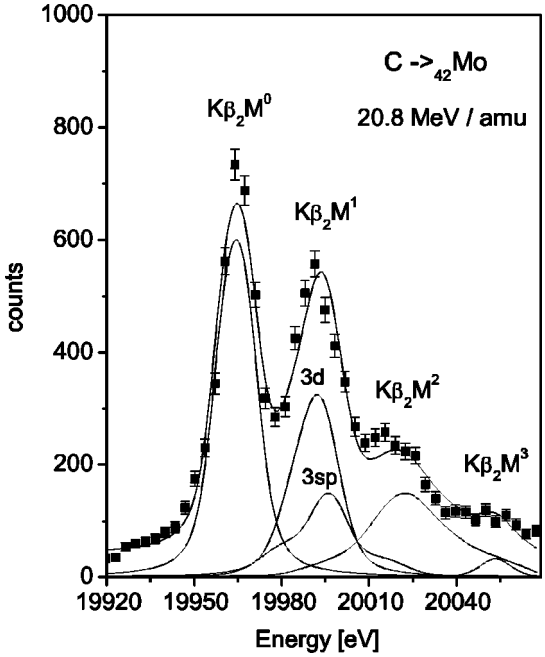

FIG. 9. Same as Fig. 7 but for Mo.

$$[I(K\beta_2\ M^1_{3d})/I(K\beta_2\ M^0)]_X$$

are the ratios derived from the fits of the ^{12}C-induced and photoinduced $K\beta_2$ spectra.

As the satellite yields concerning the photoionization measurements were taken from other sources, the photoinduced spectra could not be reanalyzed with the third step fitting procedure. For this reason, the relative subshell satellite yields were simply derived from the average M-shell satellite yields reported in Table I, assuming the relative intensities of the subshell satellites to be proportional to the

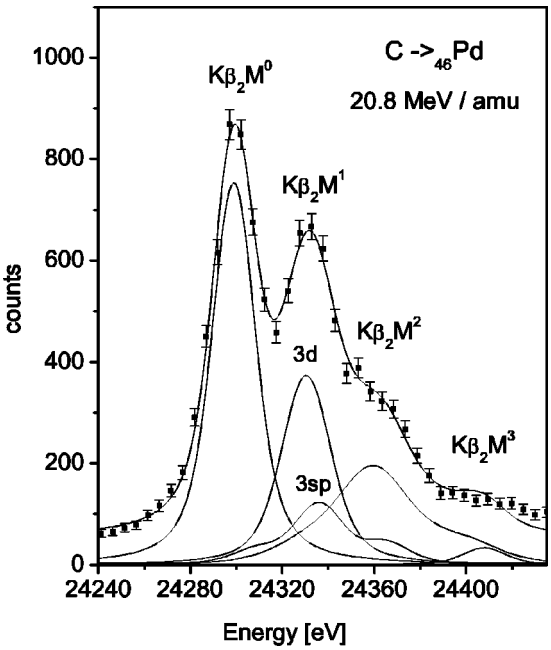

FIG. 10. Same as Fig. 7 but for Pd.

TABLE III. $X^1_{3s,3p}$ to X^0 and X^1_{3d} to X^0 x-ray yield ratios (in %) observed at the moment of the K x-ray emission as a result of collisions with 250-MeV ^{12}C ions.

Element	$X^1_{3sp}: X^0$	$X^1_{3d}: X^0$
$_{40}$Zr	42(10)	63(10)
$_{41}$Nb	32(13)	67(17)
$_{42}$Mo	35(11)[a]	61(13)[a]
$_{46}$Pd	26(13)	55(11)

[a]Taken from Ref. [63].

numbers of electrons in the different subshells. As the heavy-ion-induced yield ratios are much larger than the photoinduced ones, this approximation although crude is acceptable. The M-subshell satellite x-ray yield ratios, corrected for the shake and $K\beta_4$ transition contributions but not for the rearrangement processes are presented in Table III.

The $M_{\mathrm{I,II,III}}$ $(3s+3p)$- and $M_{\mathrm{IV,V}}$ $(3d)$-subshell ionization probabilities per electron were obtained from the corrected x-ray yield ratios listed in Table III, using first Eqs. (7) and (8) to determine the initial subshell vacancy yield ratios and then Eqs. (13) and (14) to derive the ionization probabilities. The results are presented in Tables IV and V where they are compared with SCA-HYD and SCA-DHF theoretical predictions. The SCA values were derived, using again an impact parameter $b=500$ fm. The rather big errors in the experimental probabilities originate from the uncertainties of the fitting procedure and rearrangement calculations.

We would like to point out that in spite of the fact that the M-subshell and average M-shell ionization probabilities were determined from two different fitting methods, the sets of results presented in Table II and in Tables IV and V are consistent within the quoted uncertainties. For instance, for Zr the total M-shell ionization yield derived from Table II is 0.97(20), whereas the one obtained from Tables IV and V is 0.89(13). The $(3s+3p)$ and $3d$ subshell probabilities obtained from the SCA-HYD theory are approximately equal, and hardly change with Z, for the investigated elements. They underestimate considerably the experimental data obtained in the present work, deviations up to a factor of 5 being observed. The SCA-DHF theory predicts higher ionization probabilities for the $3d$ subshells than for the $3s$ or $3p$ ones. Except for Zr, this theoretical prediction is confirmed by the present experimental results.

In general, for the SCA-DHF model a quite satisfactory agreement is found between the experimental and theoretical

TABLE IV. Experimental and theoretical (SCA model) $M_{\mathrm{I,II,III}}$-subshell ionization probabilities per electron for mid-Z targets bombarded by 20.8-MeV/amu C ions.

Element	Expt.	SCA-HYD	SCA-DHF
$_{40}$Zr	0.053(12)	0.010	0.036
$_{41}$Nb	0.040(16)	0.010	0.035
$_{42}$Mo	0.043(14)	0.011	0.034
$_{46}$Pd	0.034(17)	0.011	0.034

TABLE V. Same as Table IV but for the $M_{\mathrm{IV,V}}$ subshell.

Element	Expt.	SCA-HYD	SCA-DHF
$_{40}$Zr	0.047(9)	0.010	0.045
$_{41}$Nb	0.051(14)	0.010	0.043
$_{42}$Mo	0.046(10)	0.011	0.042
$_{46}$Pd	0.045(10)	0.011	0.045

results. Actually, as shown in Fig. 11, present experimental subshell ionization probabilities are all consistent with the SCA-DHF predictions, except for the $3s,p$ subshell of Zr for which a small but significant deviation is observed.

E. Energies of the M-shell satellites

The $K\beta_2$ M-shell satellites are shifted with respect to their parent diagram lines towards higher energies. The energy shifts depend on the hole configuration in the initial and final states of the ionized target atoms. As already mentioned, we were able to resolve experimentally the M satellite lines which correspond to zero, one, and two M-shell holes. Note that the additional N-shell ionization causes only a broadening and an asymmetry on the high-energy flanks of the observed lines. The energy shifts resulting from this additional N-shell ionization being almost the same for the diagram and M-satellite lines, the energy differences between the resolved $K\beta_2$ $L^0M^{1,2}$ satellite and $K\beta_2$ L^0M^0 diagram lines are practically not influenced by the additional N-shell vacancies.

The experimental energy shifts obtained from the first step of the data analysis (see Sec. III B) for the first- and second-order M satellites are presented in Table VI together with theoretical MCDF values computed for different configurations of the spectator vacancies. For any given transi-

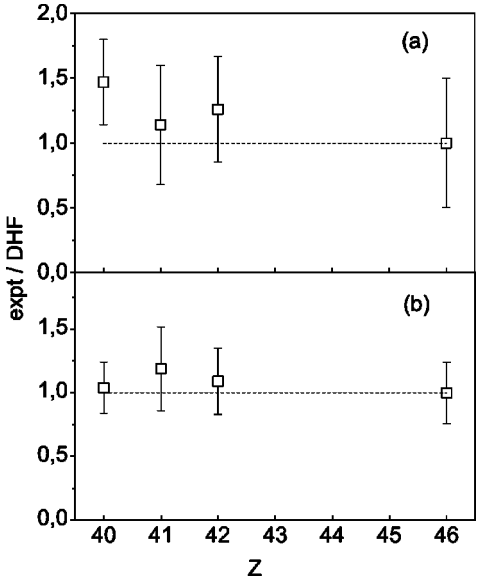

FIG. 11. Ratio of present experimental to SCA-DHF (a) $M_{\mathrm{I,II,III}}$- and (b) $M_{\mathrm{IV,V}}$-subshell ionization probabilities per electron as a function of the target atomic number for collisions with 20.8 MeV/amu C ions. The dashed lines correspond to ratios of 1.

TABLE VI. Comparison of the experimental energy shifts obtained in the present work for the $K\beta_2\ L^0M^{1,2}$ x-ray satellites with theoretical results from MCDF calculations.

Element	Expt.	SCA-HYD	SCA-DHF	
$3s^{-1}$	26.5	28.0	29.2	32.0
$3p^{-1}$	28.5	30.3	31.6	35.0
$3d^{-1}$	22.3	24.0	25.3	28.4
M^{-1}	24.8	26.5	27.7	30.9
Expt. M^{-1}	25.0(0.4)	25.7(0.5)	26.6(0.7)	32.5(0.8)
$3s^{-2}$	53.9	57.0	59.3	64.8
$3p^{-2}$	57.9	61.4	64.0	70.6
$3d^{-2}$	45.9	49.3	51.9	57.9
$3s^{-1}3p^{-1}$	55.9	59.2	61.6	67.7
$3s^{-1}3d^{-1}$	49.8	53.1	55.5	61.2
$3p^{-1}3d^{-1}$	52.0	55.4	58.0	64.3
M^{-2}	50.7	54.1	56.6	62.8
Expt. M^{-2}	51.5(0.8)	51.3(1.4)	52.6(1.8)	62.1(2.6)

tion, such as $1s^{-1}3d^{-2}\rightarrow 4p^{-1}3d^{-2}$, the theoretical energy was calculated by taking the weighted average of the energies of all MCDF components pertaining to the considered transition. The weights were calculated by multiplying the transition probabilities by the degeneracies $2J+1$ of the initial states.

The theoretical results presented in Table VI corroborate previous expectations [47,48] that the shifts in energy of K x rays are more pronounced for $3s$ and $3p$ holes than for $3d$ holes. The average theoretical energy shifts are, in general, in agreement with the experimental results within the quoted uncertainties. A detailed comparison shows, however, some discrepancies. In particular, for $_{41}$Nb and $_{42}$Mo the MCDF theory overestimates significantly the energy of the M^2 satellites. This may originate from the difficulties encountered with the MCDF calculations for multiply ionized atoms with two or more open subshells in the ground state.

Nb and Mo are indeed characterized by open $4d_{5/2}$ and $5s_{1/2}$ subshells in their ground state, whereas Zr and Pd have only one and zero open subshells in the ground state, respectively. Finally, it can be noted that the increase of the energy shifts with the atomic number is remarkably linear for both the first- and second-order satellites, confirming thus similar observations made in earlier works [67,68].

V. SUMMARY AND CONCLUSIONS

The $K\beta_2$ x-ray spectra of $_{40}$Zr, $_{41}$Nb, $_{42}$Mo, and $_{46}$Pd produced in energetic collisions with 20.8-MeV/amu ^{12}C ions were measured with a high-resolution DuMond-type curved-crystal spectrometer. The major experimental difficulty originated from the poor fluorescence yields of the $K\beta_2$ ($1s$-$4p$) transitions. These weak transitions were chosen because their M satellites can be resolved, contrary to $K\alpha_{1,2}$ and $K\beta_{1,3}$ transitions for which the energy shifts of the M satellites are smaller than the natural widths of the transitions. The intensity problem was made still worse because of the strong self-absorption of the satellite x rays in the targets, the K absorption edges falling in the same energy regions as the M satellites for the investigated elements. In spite of these severe intensity problems, the $K\beta_2\ M^1$ and $K\beta_2\ M^2$ x-ray satellites resulting from the radiative decay of $K^{-1}\ M^{-1}$ and $K^{-1}\ M^{-2}$ vacancy states could be observed and well resolved from the parent $K\beta_2\ M^0$ diagram lines. To our knowledge, this is the first observation of resolved M satellites in the heavy-ion-induced K x-ray emission of medium-Z targets.

The observed $K\beta_2$ x-ray spectra were analyzed in three steps. At first, single Voigt profiles were employed to fit the diagram and satellite lines. From this first step of the data analysis, the energy separations between the $K\beta_2\ M^{1,2}$ satellites and $K\beta_2\ M^0$ diagram lines could be determined. For both the first- and second-order satellites, an almost perfect linear dependence on the atomic number Z was found for the energy separation. The experimental results were also compared to theoretical predictions from MCDF calculations. A good agreement was observed except for the second-order M satellites of Nb and Mo for which the MCDF calculations were found to overestimate by 3–4 eV the experimental values. The deviations were explained by the questionable reliability of the MCDF calculations for atoms such as Nb and Mo that are characterized by two or more open subshells in the ground state.

In the second step of the data analysis, theoretical profiles based on extensive MCDF calculations were employed to reproduce the diagram and satellite line shapes. More accurate satellite-to-diagram yield ratios could be obtained by means of that improved fitting procedure. From the fitted yield ratios corrected beforehand to account for the atomic rearrangement processes that modify the number of M-shell vacancies prior to the K x-ray emission, we were able to derive the average M-shell ionization probabilities per electron corresponding to the investigated collisions. The obtained values were compared to theoretical predictions from the SCA model, employing SCA-HYD and SCA-DHF wave functions to describe the target atom electrons in the bound and continuum states. Whereas the SCA-HYD predictions were found to underestimate considerably the experimental probabilities, a good agreement was found between experiment and theory in the case of the SCA-DHF model. This confirms similar observations made in former experiments with lighter projectiles.

Finally, the $K\beta_2\ M^1$ satellite lines were reanalyzed using distinct MCDF profiles to fit the components corresponding to $3s,p$ and $3d$ spectator vacancies. The changes in the M-subshell vacancy configurations resulting from $M_{sp}M_dX$ Coster-Kronig transitions were included in the rearrangement calculations. From the corrected $3s,p$ and $3d$ satellite-to-diagram line yield ratios, the $M_{\mathrm{I,II,III}}$- and $M_{\mathrm{IV,V}}$-subshell ionization probabilities per electron could be determined. As for the average M-shell ionization probabilities, the experimental M-subshell ionization probabilities were found to be well reproduced by SCA-DHF calculations and in strong disagreement with SCA-HYD predictions. The latter underestimate indeed strongly the experimental results, deviations by factors comprised between 3 and 5 being observed.

ACKNOWLEDGMENTS

Partial support for this work was provided by the Polish Committee for Scientific Research (KBN) (Grant Nos. 5 P03B 077 20 and 2 P03B 094 24) and by the Swiss National Science Foundation. We also would like to thank Dr. P. A. Schmelzbach and his collaborators from the PSI Philips cyclotron staff for very good beam conditions.

[1] P.H. Mokler and F. Folkmann, in *Structure and Collision of Ions and Atoms*, edited by I.A. Sellin, Topics in Current Physics Vol. 5 (Springer-Verlag, Berlin, 1978), p. 201.

[2] J. Kawai, in *Proceedings of the Sixth International Conference on PIXE and Its Analytical Applications, Tokyo, Japan, 1992*, edited by M. Uda [Nucl. Instrum. Methods Phys. Res. B **75**, 3 (1993)].

[3] F. Folkmann, in *Proceedings of the Seventh International Conference on PIXE and Its Analytical Applications, Padua, Italy, 1995*, edited by G. Moschini and V. Valkovic [Nucl. Instrum. Methods Phys. Res. B **109/110**, 39 (1996)].

[4] B. Forslind, in *Proceedings of the Eighth International Conference on PIXE and Its Analytical Applications, Lund, Sweden, 1998*, edited by K.G. Malmqvist [Nucl. Instrum. Methods Phys. Res. B **150**, 150 (1999)].

[5] J. Hoszowska, J.-Cl. Dousse, D. Castella, D. Corminboeuf, J. Kern, Y.-P. Maillard, and P.-A. Raboud, J. Phys. B **33**, 3165 (2000).

[6] I.P. Grant, B.J. McKenzie, P.H. Norrington, D.F. Mayers, and N.C. Pyper, Comput. Phys. Commun. **21**, 207 (1980).

[7] E. Merzbacher and H.W. Lewis, in *Handbuch der Physik*, edited by S. Flugge (Springer-Verlag, Berlin, 1958), p. 166.

[8] J. Bang and J.M. Hansteen, K. Dan. Vidensk. Selsk. Mat. Fys. Medd. **31**, 13 (1959).

[9] J. Rzadkiewicz, D. Chmielewska, T. Ludziejewski, P. Rymuza, Z. Sujkowski, J. Hoszowska, D. Castella, D. Corminboeuf, J.-Cl. Dousse, B. Galley, Ch. Herren, J. Kern, M. Polasik, and M. Pajek, Phys. Lett. A **264**, 186 (1999).

[10] T.J. Grey, in *Methods of Experimental Physics*, edited by P. Richard (Academic Press, New York, 1980), Vol. 17, p. 193.

[11] K.W. Hill, B.L. Doyle, S.M. Shafroth, D.H. Madison, and R.D. Deslattes, Phys. Rev. A **13**, 1334 (1976).

[12] D. Trautmann and Th. Kauer, Nucl. Instrum. Methods Phys. Res. B **42**, 449 (1989).

[13] R.S. Sokhi and D. Crumpon, At. Data Nucl. Data Tables **30**, 49 (1984).

[14] E. Braziewicz and J. Braziewicz, J. Phys. B **21**, 1537 (1988).

[15] M. Pajek, A.P. Kobzev, and G. Lapicki, Nucl. Instrum. Methods Phys. Res. B **48**, 87 (1990).

[16] A. Bienkowski, A.P. Kobzev, R. Sandrik, A.V. Skrypnik, R.A. Ilkhamov, and G. Lapicki, Nucl. Instrum. Methods Phys. Res. B **49**, 19 (1990).

[17] M. Pajek *et al.*, Phys. Rev. A **42**, 261 (1990).

[18] A.P. Jesus and J.P. Ribeiro, Nucl. Instrum. Methods Phys. Res. A **280**, 370 (1989).

[19] G. Lapicki, J. Phys. B **23**, 3123 (1990).

[20] Ch. Herren, B. Boschung, J.-Cl. Dousse, B. Galley, J. Hoszowska, J. Kern, Ch. Rhême, M. Polasik, T. Ludziejewski, P. Rymuza, and Z. Sujkowski, Phys. Rev. A **57**, 235 (1998).

[21] M.W. Carlen, B. Boschung, J.-Cl. Dousse, Z. Halabuka, J. Hoszowska, J. Kern, Ch. Rhême, M. Polasik, P. Rymuza, and Z. Sujkowski, Phys. Rev. A **49**, 2524 (1994).

[22] T. Ludziejewski, P. Rymuza, Z. Sujkowski, B. Boschung, J.-Cl. Dousse, B. Galley, Z. Halabuka, Ch. Herren, J. Hoszowska, J. Kern, Ch. Rhême, and M. Polasik, Phys. Rev. A **52**, 2791 (1995).

[23] R. Hippler, K. Saeed, A.J. Dumcan, and H. Kleinpoppen, Phys. Rev. A **30**, 3328 (1984).

[24] S. Andriamonje *et al.*, J. Phys. B **46**, 349 (1985).

[25] M.W. Carlen, J.-Cl. Dousse, M. Gasser, J. Kern, Ch. Rhême, P. Rymuza, Z. Sujkowski, and D. Trautmann, Europhys. Lett. **13**, 231 (1990).

[26] M.W. Carlen, J.-Cl. Dousse, M. Gasser, J. Hoszowska, J. Kern, B. Perny, Ch. Rhême, P. Rymuza, Z. Sujkowski, and D. Trautmann, Z. Phys. D: At., Mol. Clusters **23**, 71 (1992).

[27] M.W. Carlen, M. Polasik, B. Boschung, J.-Cl. Dousse, M. Gasser, Z. Halabuka, J. Hoszowska, J. Kern, Ch. Rhême, P. Rymuza, and Z. Sujkowski, Phys. Rev. A **46**, 3893 (1992).

[28] D. Trautmann, F. Rösel, and G. Baur, Nucl. Instrum. Methods Phys. Res. **214**, 21 (1983).

[29] D. Trautmann and F. Rösel, Nucl. Instrum. Methods **169**, 259 (1980).

[30] Z. Halabuka, W. Perger, and D. Trautmann, Z. Phys. D: At., Mol. Clusters **29**, 151 (1994).

[31] B. Perny, J.-Cl. Dousse, M. Gasser, J. Kern, R. Lanners, Ch. Rhême, and W. Schwitz, Nucl. Instrum. Methods Phys. Res. A **267**, 120 (1988).

[32] J.A. Bearden and A.F. Burr, Rev. Mod. Phys. **39**, 78 (1967).

[33] J.L. Campbell and T. Papp, At. Data Nucl. Data Tables **77**, 1 (2001).

[34] T. Ludziejewski, P. Rymuza, Z. Sujkowski, G. Borchert, J.-Cl. Dousse, Ch. Rhême, and M. Polasik, Phys. Rev. A **54**, 232 (1996).

[35] P. Rymuza, Z. Sujkowski, M. Carlen, J.-Cl. Dousse, M. Gasser, J. Kern, B. Perny, and Ch. Rhême, Z. Phys. D: At., Mol. Clusters **14**, 37 (1989).

[36] E.J. McGuire, Phys. Rev. A **3**, 587 (1971).

[37] E.J. McGuire, Phys. Rev. A **5**, 1043 (1972).

[38] E.J. McGuire, Phys. Rev. A **5**, 1052 (1972).

[39] J.H. Scofield, At. Data Nucl. Data Tables **14**, 121 (1974).

[40] O. Keski-Rahkonen and M.O. Krause, At. Data Nucl. Data Tables **14**, 139 (1974).

[41] M.H. Chen, B. Crasemann, and H. Mark, At. Data Nucl. Data Tables **24**, 13 (1979).

[42] M.H. Chen, B. Crasemann, and H. Mark, Phys. Rev. A **21**, 436 (1980).

[43] M.H. Chen, B. Crasemann, and H. Mark, Phys. Rev. A **24**, 177 (1981).

[44] B.J. McKenzie, I.P. Grant, and P.H. Norrington, Comput. Phys. Commun. **21**, 233 (1980).

[45] I.P. Grant, Int. J. Quantum Chem. **25**, 23 (1984).

[46] K.G. Dyall, I.P. Grant, C.T. Johnson, F.A. Parpia, and E.P.

Plummer, Comput. Phys. Commun. **55**, 425 (1989).
[47] M. Polasik, Phys. Rev. A **39**, 616 (1989).
[48] M. Polasik, Phys. Rev. A **52**, 227 (1995).
[49] M. Polasik, Phys. Rev. A **39**, 5092 (1989).
[50] M. Polasik, Phys. Rev. A **40**, 4361 (1989).
[51] M. Polasik, Phys. Rev. A **41**, 3689 (1990).
[52] G. Raisbeck and F. Yiou, Phys. Rev. A **4**, 1858 (1971).
[53] G. Lapicki and W. Losonsky, Phys. Rev. A **15**, 896 (1977).
[54] G. Lapicki and F.D. McDaniel, Phys. Rev. A **22**, 1896 (1980).
[55] V.S. Nikolaev, Zh. Ekso. Teor. Fiz. **51**, 1263 (1966) [Sov. Phys. JETP **24**, 847 (1967)].
[56] T.A. Carlson and M.O. Krause, Phys. Rev. **140**, 1057 (1965).
[57] T. Aberg, Phys. Rev. **156**, 35 (1967).
[58] M.O. Krause, T.A. Carlson, and R.D. Dismuke, Phys. Rev. **170**, 37 (1968).
[59] T.A. Carlson and C.W. Nestor, Phys. Rev. A **8**, 2887 (1973).
[60] L.G. Parrat, Rev. Mod. Phys. **31**, 616 (1959).
[61] J.-Cl. Dousse and J. Hoszowska, Phys. Rev. A **56**, 4517 (1997).
[62] J. Hoszowska and J.-Cl. Dousse, J. Phys. B **29**, 1641 (1996).
[63] J. Rzadkiewicz, D. Chmielewska, T. Ludziejewski, P. Rymuza, Z. Sujkowski, J. Hoszowska, D. Castella, D. Corminboeuf, J.-Cl. Dousse, B. Galley, Ch. Herren, J. Kern, M. Polasik, and M. Pajek, Nucl. Instrum. Methods Phys. Rev. B (to be published).
[64] M. Pajek, A.P. Kobzev, D. Trautmann, and Th. Kauer, Nucl. Instrum. Methods Phys. Res. B **52**, 109 (1990).
[65] J.M. Hansteen, L. Kocbach, and A. Graue, Phys. Scr. **31**, 63 (1985).
[66] E. Braziewicz *et al.*, J. Phys. B **24**, 1669 (1991).
[67] D. Burch, L. Wilets, and W.E. Meyerhof, Phys. Rev. A **9**, 1007 (1974).
[68] I. Török, T. Papp, and S. Raman, Nucl. Instrum. Methods Phys. Res. B **150**, 8 (1999).